

Nitrogen-monovacancy (V_N) Hexagonal Boron Nitride 2D Monolayer Material as an Efficient Electrocatalyst for CO_2 Reduction Reaction

Lokesh Yadav¹ and Srimanta Pakhira^{1,2*}

¹ Theoretical Condensed Matter Physics and Advanced Computational Materials Science Laboratory, Department of Physics, Indian Institute of Technology Indore (IIT Indore), Simrol, Khandwa Road, Indore-453552, Madhya Pradesh, India.

² Theoretical Condensed Matter Physics and Advanced Computational Materials Science Laboratory, Centre for Advanced Electronics (CAE), Indian Institute of Technology Indore, Simrol, Khandwa Road, Indore-453552, Madhya Pradesh, India.

*Corresponding author: spakhira@iiti.ac.in (or) spakhirafsu@gmail.com

Abstract

The conversion of waste carbon dioxide (CO_2) gas into valuable products and fuels through an electrocatalytic CO_2 reduction reaction (CO_2RR) is a promising approach. The sluggish kinetics of the CO_2RR require the development of novel strategies for electrocatalyst design. Two-dimensional (2D) materials emerge as promising candidates for CO_2RR due to their distinctive electronic and structural properties. This study follows the first principles based DFT-D method to examine the electrocatalytic competences of the defective two-dimensional boron nitride monolayer (d-BN) material towards CO_2RR . Introducing a particular defect with nitrogen vacancies in the 2D single layer pristine hexagonal boron nitride (V_N -d-BN) can efficiently activate the CO_2 molecules for hydrogenation by reducing the electronic band gap of the pristine hBN from 6.23 eV to 3.0 eV. Therefore, V_N -d-BN material can act as a large band gap semiconductor. Our findings demonstrate that the defective regions in the 2D monolayer V_N -d-BN serve as active sites (Boron) for both the adsorption and activation of CO_2 . The subsequent hydrogenation steps occur sequentially once the CO_2 molecule is adsorbed on the catalytic surface. Our results indicate that the OCHO* path is the most

favorable for CH₄ production. Hence, the 2D monolayer V_N-d-BN material holds a great promise as a cost-effective catalyst for CO₂RR, and it presents a viable alternative to expensive platinum (Pt) catalysts.

Introduction

The rapid growth of industrialization leads to technological advancements in our daily lives, but it also raises significant environmental concerns, primarily due to the increasing pollution levels. The primary source of this increasing pollution level is the combustion of fossil fuels, which alternatively intensifies the CO₂ emissions into our environment and subsequent climate change.¹⁻³ Various strategies have been developed to control the unnecessary production of CO₂ emissions, such as minimizing fossil fuel usage by adopting alternate renewable energy sources. An electrochemical CO₂RR is considered one of the most promising techniques for transforming CO₂ into valuable products such as methanol (CH₃OH), methane (CH₄), and formic acid (HCOOH) under room temperature and ambient pressure conditions.⁴⁻⁷ This significant step towards this endeavor for electrochemical conversion of CO₂ into valuable products attracts the scientific community for future challenges. Integrating electrochemical CO₂RR into renewable energy sources holds the promise of establishing a carbon-neutral energy cycle.

Over the past decades, researchers have extensively explored photochemical, thermochemical, and electrochemical methods for CO₂ reduction.⁸⁻¹² Thermochemical conversion, which relies on high temperatures, pressures, and equivalent amounts of hydrogen as a reducing agent, makes it impractical for large-scale applications due to energy constraints.^{7,12} In the photochemical processes, a few catalysts have shown some activity in CO₂RR, but their selectivity and production rates are prohibitively low from an economic perspective.^{8,10} In contrast, electrochemical CO₂RR holds various advantages.^{11,13-15} One of the advantages is that it can perform under ambient conditions, and we can precisely control the rate of reaction by adjusting the external bias. Also, the products are generated at the different electrodes, naturally facilitating the separation of products using the individual reaction chambers.¹⁶ This feature reduces the cost of post-reaction separation processes, making electrochemical CO₂RR a sustainable option. However, several challenges remain in the field of electrochemical CO₂RR, including high overpotential, low selectivity, and low yields resulting from the thermodynamical stability of CO₂. Furthermore, the use of CO₂

electrocatalysis is limited due to the excessive costs and inaccessibility of novel metal catalysts such as Pt, Au, and Pd.¹⁷ Many efforts have been made to develop novel, feasible, and efficient electrocatalytic materials that can accomplish high rates of CO₂RR with low overpotential as one of the solutions to these issues. Numerous 2D nanosheets can show promise for the reduction of CO₂, depending on the preferred reaction products such as CO, HCOOH, CH₃OH, and CH₄.

The research on 2D nanosheets following the discovery of graphene has expanded significantly over the past decade, and various 2D materials have been identified, such as covalent organic frameworks, chalcogenides, oxides, nitrides, halides, carbides, hydrides, hydroxides, phosphonates, phosphates, metals, and elements from groups IV and V.¹⁸ These 2D materials can exhibit insulating, semiconducting, and metallic properties. Notably, when multi-layered materials are reduced into a monolayer, they exhibit enhanced and novel electronic characteristics due to quantum confinement. Additionally, 2D materials offer a high specific surface area due to their reduced dimensionality. Different methods, such as doping, intercalation, alloying, and chemical functionalization, help us tune the physicochemical properties of 2D materials.¹⁸ These strategies enhance the opportunities to design nanosheets for catalysis as well as energy applications. Catalysis of the 2D nanosheets has gained considerable attention due to their distinctive structural and electronic properties.¹⁹ These ultrathin nanosheets possess exposed surface atoms on both sides and can escape the lattice to create vacancy-type defects. The presence of vacancy defects in nanosheets can result in the reduction of the coordination number of surface atoms, ultimately boosting catalytic performance. Also, the increment in low-coordinated surface sites enhances the chemisorption of reactants. Controlling vacancy defects can help us to modify the catalytic activities and the corresponding electronic structure. Moreover, the atomic sites present at the low coordinated edges of nanosheets exhibit intriguing catalytic properties.

The remarkable properties of 2D materials (especially hexagonal boron nitride (hBN)) have gained significant attention in various scientific fields. For example, the 2D material hBN has numerous applications, such as biomedical devices, power devices, fuel cells, dielectric tunnelling, stretchable optoelectronic devices, and electrocatalytic water splitting.^{20–24} The geometrical structure of hBN closely resembles graphite. A monolayer of hBN can be simulated by substituting all the carbon atoms present in graphene with boron (B) and nitrogen (N) atoms.²⁵ The alternating B/N atoms are covalently bound into a hexagonal layer, and weak van

der Waals forces hold these layers together. Unlike graphite, hBN exhibits a distinct interlayer stacking pattern where B atoms align directly below or above the N atoms in adjacent layers. This configuration indicates the polar nature of B-N bonds due to the distinct electronegativity of B and N atoms, inducing a partial ionic character within these covalent bonds.²⁶ Due to the higher electronegativity of the N atoms, the electron pairs in sp^2 -hybridized B-N σ bonds are confined to the N atoms. The pristine hBN exhibits exceptional stability, a flat surface, and insulating behavior with a relatively wide bandgap ranging from 3.60 eV to 7.0 eV, depending on the use of experimental methods.²⁷⁻³⁰ This wide bandgap of the material is a challenge for utilizing hBN-based materials as efficient electrocatalysts for the CO₂RR.

Several strategies, such as metal doping, functional group adsorption, and hydrogenation, have been explored to enable effective electronic communication with the hBN surface.^{31,32} Unfortunately, these approaches often lead to structural deformations in the pristine 2D planar geometry of hBN due to a mismatch between the size of the metal atom and the B/N atom. Consequently, these modifications may compromise the desired properties of hBN. The hBN material exhibits considerable potential due to its robust chemical stability, making it a noteworthy material explored across various domains, including nitrogen reduction reaction (NRR), CO₂ reduction reaction, and CO oxidation.³³⁻³⁸ Chen et al. explored a number of metal-loaded BN, revealing that MoN₃/BN is a standout performer in NRR by strategically replacing a B atom with Mo on hBN.³⁸ Ajayan et al. utilized porous hBN as a substrate, employing a one-step vacuum filtration process to successfully fabricate a monoatomic Ru/hBN catalyst for the CO₂RR.³⁵ Furthermore, the defects induced in hBN significantly reduce the band gap, enhancing electrical conductivity to process electrochemical reactions. In other words, it has been observed that the 2D monolayer hBN, in the presence of vacancy defects, gives rise to semiconducting essence.

The 2D pristine hBN nanomaterial cannot be used effectively as an electrocatalyst for the CO₂RR due to its wide electronic band gap (E_g), showing its electrical insulating behavior. Due to the lack of a sufficient number of active catalytic sites, it hinders the practical use of catalytic reactions. A recent experiments performed by Yu Lei et al. demonstrated various vacancies or defects in the pristine 2D single layer hBN material (noted by d-BN), and they found that the presence of different types of vacancies within d-BN induces substantial changes in its band structure and causes a shift in the Fermi energy (E_F) level.³⁹ Furthermore, spin density calculations and electron spin resonance (ESR) experiments provided a theoretical and experimental confirmation of generating localized free radicals in these vacancies.³⁹ In another

study, Katerina L. et al. experimentally showed that the 2D monolayer d-BN with nitrogen defects can activate the CO₂ molecule for hydrogenation, and the d-BN sheet can potentially serve as an active electrocatalyst for CO₂RR.⁴⁰ They found that the d-BN with nitrogen defect catalyzes formic acid and methanol formation at different temperatures.⁴⁰ To support and explain the experimental observation, , we have computationally performed our calculations under standard conditions (T = 298.15 K, p = 1 bar, U = 0 V, and pH = 0).

We have theoretically designed a 3x3 supercell of a 2D pristine hBN sheet and introduced a specific defect in this sheet with a single nitrogen-vacancy (V_N), forming a nitrogen defective 2D monolayer boron nitride material noted by V_N _d-BN. After that, we studied the electronic and geometrical properties of this material by employing first-principles based dispersion-corrected density functional theory method (DFT-D). This V_N vacancy defect has rendered V_N _d-BN material chemically active. The formation of 2D monolayer V_N _d-BN material from the 2D single layer pristine hBN is depicted in Fig. 1. Using the same DFT-D approach, we calculated the electronic properties such as the electronic band structure, total density of states (DOS), electronic band gap (E_g), and position of the Fermi energy level (E_F) to study the properties of the V_N _d-BN material with their CO₂RR mechanism precisely. We also performed electron spin density calculations to locate the presence of unpaired electrons in the system. In our previous work, we found that the calculated electronic band gap of the 2D monolayer pristine hBN was about 6.23 eV, but in our current study, we have found that it is reduced to 3.0 eV after introducing the V_N vacancy defect to the pristine hBN which is consistent with the previous study.⁴¹ This reduction in the band gap indicates a novel strategy to improve the CO₂RR performance of the V_N _d-BN material which is well harmonized with the experimental observation.⁴⁰ We investigated the CO₂RR mechanism on the surface of 2D single layer V_N _d-BN material. Our research thoroughly examined how CO₂ is converted into various products on the catalytic surface using a first principles-based DFT-D approach which explain the experimental results obtained by Chagoya et al.⁴⁰ We carefully analyzed the adsorption configurations of CO₂ and its intermediates during the CO₂RR process by calculating the changes in Gibbs free energy (ΔG). Our calculations outlined the essential stages of hydrogenating CO₂ into C1 products, such as CO, HCOOH, CH₃OH, and CH₄, indicating that the 2D monolayer V_N _d-BN material exhibits higher CO₂RR selectivity towards CH₄ formation. The findings of this study confirm that the 2D monolayer V_N _d-BN can efficiently serve as an electrocatalyst for the CO₂RR.

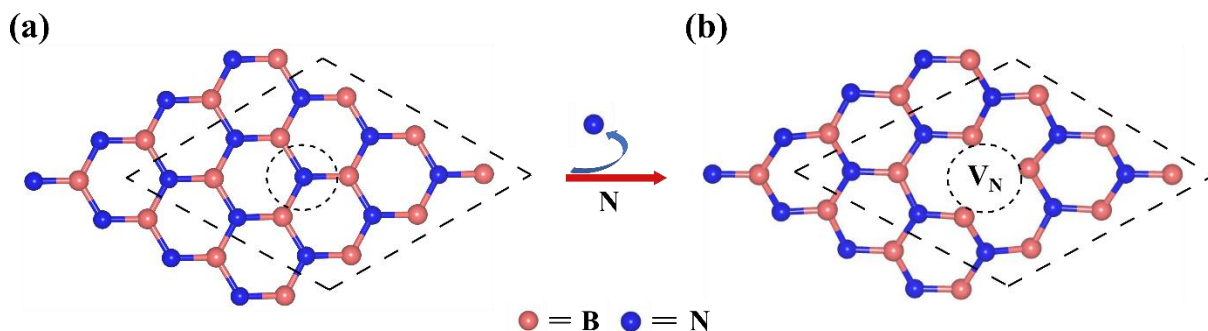


Fig. 1 Equilibrium structures of (a) the pristine 2D monolayer hBN and (b) the 2D monolayer V_N -d-BN materials. (The dotted lines represent the boundary of 3×3 supercells.)

Theoretical Methodology and Computational Details

(a) Methodology

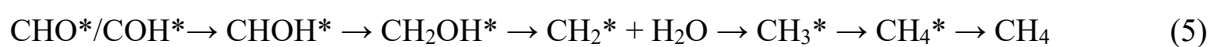
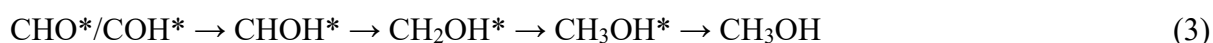
We investigated the equilibrium structures and properties of the 2D monolayer V_N -d-BN material by employing a periodic hybrid dispersion-corrected first principles-based B3LYP-D3 density functional theory (DFT-D) method, which.^{42–45} We performed these calculations by using *ab initio* based CRYSTAL17 suite code, which employs Gaussian types of atomic basis sets during the computations. It is more efficient than plane wave-based codes for hybrid DFT-D calculations.^{46–51} We used specific Gaussian basis sets with triple- ζ valence and polarization quality (TZVP) for oxygen (O), hydrogen (H), carbon (C), boron (B), and nitrogen (N) atoms in the present investigation. Due to weak van der Waals (vdW) interactions among the atoms within the layers of V_N -d-BN nanosheet, we have also considered the significance of vdW dispersion effects. To address long-range vdW interactions, Grimme's 3rd order (-D3) corrections were incorporated in these computations.⁵² The B3LYP-D3 method is helpful in providing reliable and appealing geometries for the monolayer 2D structures because energy and density have the minimum effect of spin contamination in our calculations, where we set the electronic self-consistency scale to 10^{-7} atomic units. Two-dimensional vacuum slabs were constructed for the materials to incorporate the electrostatic potential in the computations. We take energy calculations with respect to the vacuum where the height of the vacuum cell is set at 500 Å. We employed a $4 \times 4 \times 1$ Monkhorst–Pack k-mesh grid where we sampled all integrations of the first Brillouin zone.⁵³ We have set a 10^{-7} a.u. threshold for convergence of energy and electron density. We have also used the (VESTA) visualization code for the graphical analysis of all the optimized structures.⁵⁴

(b) CO₂RR mechanism

In the CO₂RR process, electrons move toward the cathode through an external circuit, and each electron, together with a proton, reaches toward the CO₂ molecule and makes a bond with the carbon or oxygen atom, forming various products. These products can be formic acid (HCOOH), carbon monoxide (CO), methanol (CH₃OH), and methane (CH₄), based on the paths followed. The primary two-electron (2e⁻) reduction products in CO₂RR are carbon monoxide (CO) and formic acid (HCOOH), as shown in eqn. (1) and (2). Initially, the hydrogenation of adsorbed CO₂ molecule results in the formation of either COOH* or OCHO*, which can further be reduced to CO* or HCOOH*, respectively. As illustrated in the equations below, the intermediates CO* and HCOOH* can then leave the catalyst surface, and one can get CO and HCOOH molecules as final products, respectively, during CO₂RR. Here “*” represents the active site on the surface of the catalyst.



The further hydrogenation of adsorbed CO* to COH* or CHO* can lead to the generation of CH₃OH and CH₄ molecules as the six-electron or eight-electron reduction products, respectively. To produce a CH₃OH molecule as a final product, eqn. (3) presents the pathway where initially CHO*/COH* reduced to CHOH*, which further reduced to CH₂OH*. Finally, *CH₂OH is reduced to give CH₃OH as the ultimate product.



The formation of a CH₄ molecule as a final product can occur through three possible routes, as shown in eqn. (4), (5), and (6). Eqn. (4) involves the initial reduction of CHO* or COH* to CHOH*, followed by hydrogenation to CH* intermediate and H₂O molecule. Subsequently, CH* undergoes further reduction to CH₄ through a series of hydrogenation steps. However, it is important to emphasize that the hydrogenation of CHOH* to the formation of CH* intermediate usually presents a high energy barrier compared to the formation of CH₂OH* and OCH₃* intermediates, which indicates that the path in eqn. (4) is less favorable than that

mentioned in eqn. (5) and (6) when the CO₂RR takes place on the catalytic surface. In eqn. (5), the intermediate CHO* or COH* is initially reduced to CHOH*, which further hydrogenates to CH₂OH* and then generates a CH₂* intermediate along with a water molecule. Next, the CH₂* intermediate undergoes hydrogenation to CH₃*, producing CH₄ as a final product which leaves from the catalyst surface. On the other hand, eqn. (6) presents an alternative path where CHO* is reduced to OCH₂* and further undergoes hydrogenation to form an OCH₃* intermediate. The OCH₃* intermediate is further reduced into a CH₄ molecule in the next step, leaving a single oxygen atom (O*) on the catalytic surface. Eventually, the remaining O* on the catalytic surface is reduced to OH*, and at last, during further hydrogenation, an H₂O molecule is produced as a final product.

(c) Thermodynamic analysis and energy calculations

The DFT-D approach was consistently applied throughout the calculations to accurately account for the changes in Gibbs free energy (ΔG) during the CO₂RR process. The catalytic performance of the V_N_d-BN material in the CO₂RR was studied by computing the change in Gibbs free energy (ΔG) for each intermediate species involved in the subject reaction. We use the *Computational Hydrogen Electrode* (CHE) model to determine the values of ΔG of each intermediate species during the CO₂RR process. We performed all of these calculations under standard conditions (T = 298.15 K, p = 1 bar, U = 0 V, and pH = 0). We have followed the method proposed by Nørskov et al., which demonstrated that the chemical potential of a sum of both electron and proton (H⁺ + e⁻) can be correlated with the chemical potential of ½ H₂ molecule in the gaseous state utilizing the standard hydrogen electrode.⁵⁵ Here, we use this correlation under standard conditions to calculate the energy change for the hydrogenation in each reaction step of CO₂RR. We calculated the change in adsorption energies (ΔE) by determining the energy difference between the model with the adsorbed species [$E_{\text{slab} + \text{adsorbate}}$], the catalytic model V_N_d-BN [$E_{\text{adsorbent}}$], and the adsorbate itself [$E_{\text{adsorbate}}$], as given below:

$$\Delta E = E_{\text{slab} + \text{adsorbate}} - (E_{\text{adsorbent}} + E_{\text{adsorbate}})$$

The negative value of change in adsorption energy represents the stability of intermediates on the catalytic surface, indicating that the adsorbate is energetically bound to the surface of V_N_d-BN material. Hence, this negative value of change in adsorption energy is favorable for elementary reactions on the surface of V_N_d-BN. Additionally, we computed the changes in Gibbs free energy (ΔG) for each reaction step of the CO₂RR occurring on the surface of V_N_d-BN material using the following equation:

$$\Delta G = \Delta E + \Delta E_{\text{ZPE}} - T\Delta S + \Delta G_{\text{pH}}$$

Here, ΔE represents the change in adsorption energy, ΔE_{ZPE} represents the zero-point energy, ΔS is the entropy correction (differences between the gas phase and the adsorbed state), and T represents the temperature of the system (we considered here room temperature ($T = 298.15$ K) for this work). The term ΔG_{pH} represents the Gibbs free energy change resulting from changes in H^+ concentration in an acidic medium, and for this study, we set a zero value to the term ΔG_{pH} .

Results and discussions

To investigate the CO_2RR mechanism, we computationally designed a 3×3 supercell of a 2D monolayer pristine hBN sheet containing totally number of nine B atoms and nine N atoms. Then, we introduced a single nitrogen-vacancy defect (V_{N}) in this 2D monolayer pristine hBN sheet to form a 2D monolayer $V_{\text{N}}\text{-d-BN}$ material. The equilibrium structures of both the 2D pristine hBN and $V_{\text{N}}\text{-d-BN}$ materials are shown in Fig. 1a and 1b, respectively. In our recent previous work, we already discussed both the structural and electronic properties of the pristine 2D monolayer hBN material in detail.⁴¹ Recent studies have demonstrated that introducing vacancy defects modifies the physiochemical and electronic structure of materials, improving electrocatalytic performance through defect engineering.³⁹⁻⁴¹ The catalytic activity of the d-BN depends on the distribution and position of defects within the structure. It is already experimentally and theoretically confirmed by ESR and spin density calculations that these defects generate localized free radicals.³⁹ We studied the structural and electronic properties of the 2D monolayer $V_{\text{N}}\text{-d-BN}$ material to analyze the electrocatalytic performance towards the CO_2RR . The electronic properties, i.e., electronic band structure and total density of states of the 2D monolayer $V_{\text{N}}\text{-d-BN}$ material are shown in Fig. 7a. Our current DFT-D analysis indicates the values of lattice constants calculated to be $a = 7.285$ Å, $b = 7.438$ Å along with the interfacial angles $\alpha = \beta = 90^\circ$ and $\gamma = 119.32^\circ$ with the P1 symmetry. The $V_{\text{N}}\text{-d-BN}$ sheet exhibits an electronic band gap of 3.0 eV, which results in a large band gap semiconductor material. The reduced electronic bandgap of $V_{\text{N}}\text{-d-BN}$ material raises the electron concentration and improves the conductivity to perform CO_2RR . It may be helpful to facilitate the electron transfer toward reactants in CO_2RR processes. It offers a novel strategy for effectively utilizing the $V_{\text{N}}\text{-d-BN}$ material to perform the CO_2RR . Consequently, we expect this 2D monolayer $V_{\text{N}}\text{-d-BN}$ material to demonstrate an improved electrocatalytic activity for CO_2RR .

The vibrational stability of a system is a crucial aspect determining its overall stability, especially in relaxed configurations. Raman spectroscopy provides valuable insight into the vibrational modes of molecules of materials, offering a detailed picture of their structural dynamics. Under the DFT-D approaches, we use the B3LYP-D3 method implemented in the CRYSTAL17 suite code to simulate the Raman spectrum, which helps us to study the stability of a system, Raman active frequencies, and amplitudes of vibrational modes under various conditions. For these calculations, we have used a set of $4 \times 4 \times 1$ Monkhorst–Pack k-point grids. We have performed the harmonic vibrational analysis with thermochemistry at room temperature ($T = 298.15$ K) to check the thermal stability of the system. This harmonic vibrational analysis of the equilibrium structure of both the 2D monolayer pristine hBN and V_N _d-BN materials help to study Raman spectra. Fig. 2 shows the simulated Raman spectrum for both (a) hBN and (b) V_N _d-BN materials. In the simulated Raman spectrum of the pristine 2D single layer hBN, two distinct peaks are observed at wavenumbers 877.77 cm^{-1} and 1372.35 cm^{-1} , obtained by the DFT-D method. We have also identified two intense peaks for the simulated Raman spectrum of the 2D single layer V_N _d-BN material. One of these peaks corresponds to a vibrational mode (ν_1) occurring at a wavenumber of 1422.21 cm^{-1} , considered as a reference with 100% intensity. The second vibrational mode (ν_2) appears at 1338.39 cm^{-1} and exhibits approximately 98% of the intensity of the highest Raman active vibrational mode ν_1 . We have also observed other vibrations to the left of this intense peak, but their intensity is less than the ν_1 vibrational mode. The range of these vibrations is around 50–80% of the intensity of the ν_1 mode. The Raman active spectrum spread from 100 to 1550 cm^{-1} in this case. However, all other vibrations are comparatively less intense, falling below 50% of the intensity of ν_1 .

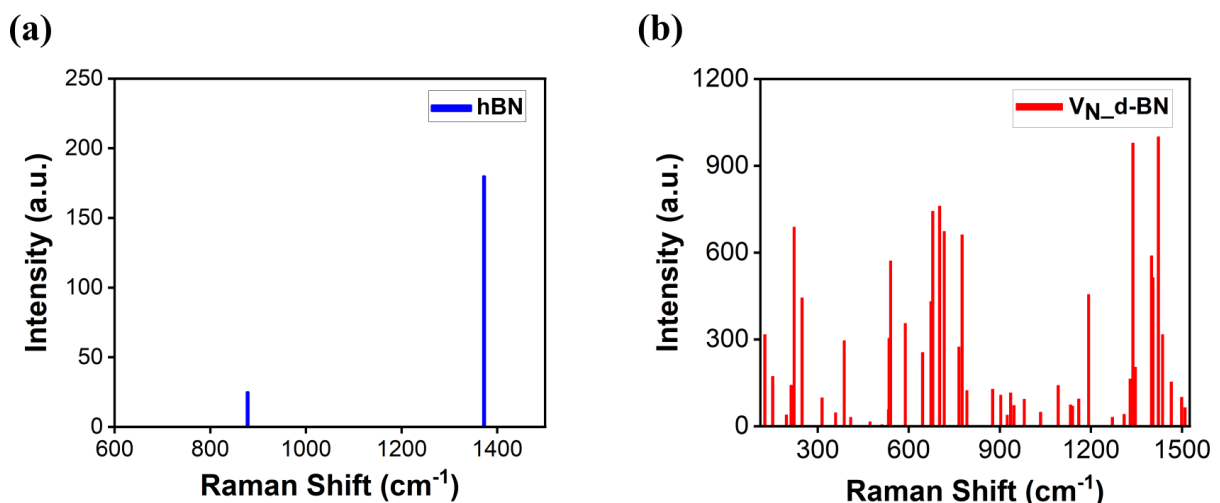


Fig. 2 Simulated Raman spectra of the (a) pristine 2D monolayer hBN and (b) 2D monolayer V_N -d-BN materials are shown here.

After determining the stable configuration, electronic structure, geometry, and electronic properties of the V_N -d-BN material, we have explored how effective this V_N -d-BN material is as an electrocatalyst for CO_2 RR. The primary objective of this work is to examine the potential of this V_N -d-BN sheet as an efficient electrocatalytic material for the CO_2 RR. In this study, we have explored various possible reaction pathways and primary reduction products involved in the CO_2 RR utilizing the periodic 2D slab structure of the V_N -d-BN material, which is based on the computational hydrogen electrode (CHE). The complete CO_2 RR process includes multiple reaction steps with various intermediates. By studying numerous adsorption sites, we have identified the most stable adsorption structures of the reaction intermediates. In our analysis, we have only focused on the formation of single-carbon intermediates and products such as HCOOH, CO, CH_3OH , and CH_4 . Here, by following an experimental work by Katerina L. et al., we have excluded all other possibilities of the formation of multi-carbon compounds.⁴⁰ The main objective of the present theoretical work is to explain the experimental observation performed by Katerina L. et al.⁴⁰ During each hydrogenation step, several CO_2 RR routes can exist where the H can adsorb on the C or O atom. In this present study, we have discussed the most favorable reaction path of CO_2 RR towards various intermediates and products in detail. We have calculated the change in Gibbs free energies for all considered paths, helping us to understand the complete reduction process and determine the optimal path and final achievable products on the surface of the V_N -d-BN electrocatalyst.

The adsorption of linear CO_2 molecules is challenging because CO_2 is fully oxidized and thermodynamically stable. So, in most of the cases, it cannot be absorbed effectively and spontaneously on the catalytic surface. Therefore, we have considered the adsorption and activation of CO_2 molecules on the surface of the catalysts as the first step of CO_2 RR. Usually, this process requires electron injection into the antibonding $2\pi_u$ orbitals of the CO_2 molecule. Therefore, the 2D monolayer V_N -d-BN can capture the CO_2 molecule effectively due to its large number of exposed active sites with the improved electron transfer capacity due to free radicals. In the most stable adsorption configuration of the CO_2 molecule, one of the oxygen and carbon atoms are bonded with two active sites (Boron), as shown in Fig. 3a. When CO_2^* interacts with the V_N -d-BN material at its surface, the C-O bond length significantly increases from 1.160 Å to 1.292 Å obtained by the DFT-D method. After the adsorption of CO_2^* onto

the V_N _d-BN surface, the equilibrium bond lengths for B-C, B-O, and C-O are found to be 1.591 Å, 1.392 Å, and 1.292 Å, respectively, as reported in Table 1. Now, the linear structure of the CO_2 molecule transforms to a V-shape structure with an angle of 120.29° . This transformation indicates that the V_N _d-BN material effectively activates the CO_2 molecule. The value of ΔG during this reaction step is approximately -0.92 eV, as reported in Table 2, indicating an exothermic nature of the reaction and, hence, thermodynamically favorable. Therefore, the negative value of change in Gibbs free energy of adsorption of CO_2^* favors the stability of the reaction on the catalytic surface. The optimized lattice parameters, space group symmetry, electronic band gap, and average bond lengths for the CO_2 adsorption on the surface of the 2D monolayer V_N _d-BN material under equilibrium conditions are presented in Table 1.

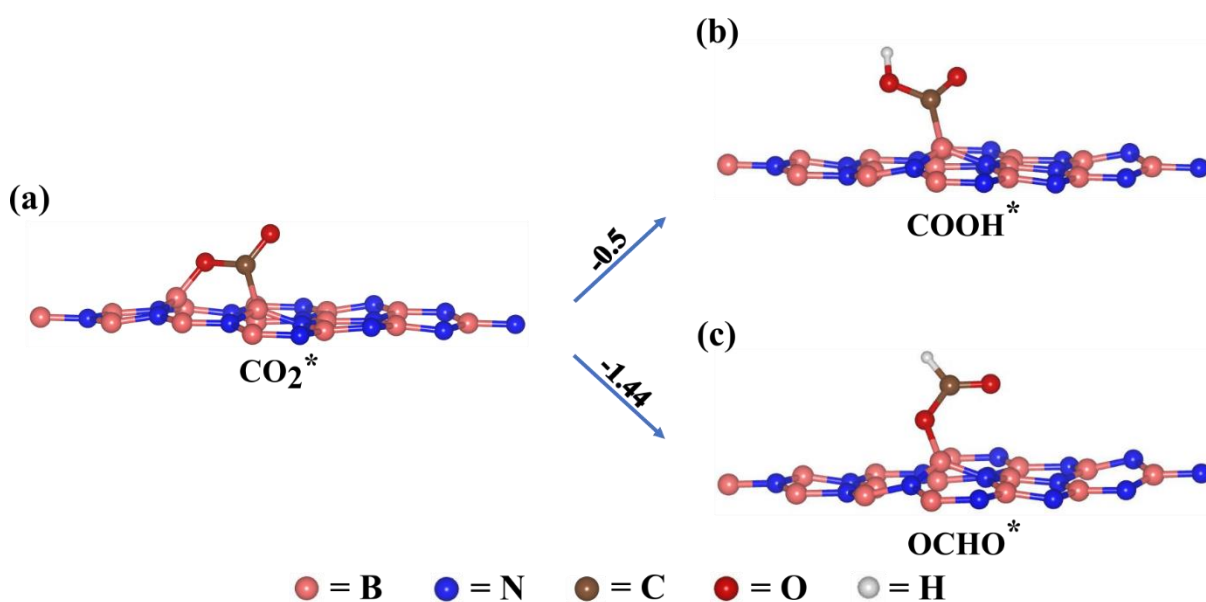


Fig. 3 Adsorption of CO_2 molecule and formation of $COOH^*$ and $OCHO^*$ intermediates on the surface of V_N _d-BN material with the optimized structures of (a) CO_2^* , (b) $COOH^*$, and (c) $OCHO^*$.

After the successful adsorption of the CO_2 molecule, the first stage of hydrogenation of the adsorbed CO_2 molecule can take place either on the C or O site, resulting in the formation of a stable carboxyl group ($COOH$) or formate group ($OCHO$) intermediates, respectively. Fig. 3 shows the optimized structures of both the $COOH$ and $OCHO$ intermediates formed during the CO_2RR on the surface of V_N _dBN material. The initial hydrogenation step is crucial in determining the overall reaction path of CO_2RR . In this study, we have extensively examined paths of both the $COOH$ and $OCHO$ intermediates for producing formic acid ($HCOOH$),

methanol (CH₃OH), and methane (CH₄). The potential energy surface diagram (as depicted in Fig. 6) i.e., reaction pathway shows the relative Gibbs free energies for both the considered paths of CO₂RR on the surfaces of the 2D V_N_d-BN material. It also shows the formation of different intermediates and products with C1 species according to the number of hydrogenation steps for both CO₂RR paths.

CO₂RR through the COOH path

The formation of COOH* on the surface of V_N_d-BN material occurred through the first hydrogenation step at the O site of the adsorbed V-shaped CO₂ molecule as depicted in Figure 3a. Fig. 4 shows the equilibrium structures of all these intermediates of the COOH path with their corresponding values of ΔG . The hydrogenation at the O site does not significantly change the CO₂ hydrogenation structure. During this hydrogenation step, the B-O bond splits, and a new O-H bond is formed on the catalytic surface, forming a COOH* intermediate, as shown in Fig. 3b and 4a. In this elementary reaction step, we observed a ΔG value of -0.5 eV for the COOH* formation on the surface of the 2D monolayer V_N_d-BN material. The negative value of ΔG indicates that the reaction step is exothermic and spontaneous. In the second hydrogenation step, the hydrogen can bond with a C or O atom of the COOH* intermediate. If the hydrogen bonds with the oxygen atom located distantly from the surface, it produces an H₂O molecule, which leaves the catalytic surface, and only CO* remains on the surface of V_N_d-BN material, as shown in Fig. 4c. In this step, we observed a value of ΔG around -1.67 eV. The higher negative value of ΔG indicates that hydrogen can strongly bind to the surface of V_N_d-BN material, making the desorption step difficult. On the other hand, if hydrogen bonds with the carbon atom, it leads to the formation of HCOOH* intermediate on the surface of V_N_d-BN material, as depicted in Fig. 4b. This reaction step shows a positive value of ΔG around 1.87 eV. This higher positive value of ΔG signifies a weak hydrogen binding on the surface of V_N_d-BN material, which will create difficulty in adsorption. The negative value of ΔG for CO* formation confirmed the exothermic nature of the reaction, so it occurs spontaneously on the surface of V_N_d-BN material. In contrast, the positive value of ΔG for HCOOH* formation indicates the endothermic nature of the reaction, so we require energy for hydrogenation on the catalytic surface. Here, we consider the CO* formation due to its negative value of ΔG for further hydrogenation. The CO* intermediate plays a crucial role in the CO₂RR as its ability to adsorb on a catalyst strongly influences whether CO becomes the primary

product or undergoes additional hydrogenation. If the value of ΔG for forming the CO^* is small, it will desorb as a CO molecule from the catalytic surface as the final product. However, if the value of ΔG for forming the CO^* on the surface of V_N -d-BN material is moderate, it will more favorably generate final products containing more than two electrons, such as CH_3OH and CH_4 . Here, the value of ΔG is around -1.67 eV, indicating that CO^* hydrogenates in further reaction steps to produce CH_3OH or CH_4 as a final product.

In the third hydrogenation step, the adsorbed CO^* molecule undergoes further hydrogenation to yield COH^* and CHO^* rather than undergoing desorption. On the V_N -d-BN surface, the value of ΔG required for CO^* hydrogenation to form CHO^* intermediate is 1.98 eV, as shown in Fig. 4d. In contrast, the value of ΔG required for CO^* hydrogenation to form COH^* intermediate is 4.32 eV, as shown in Fig. 4e. The positive value of ΔG for both cases indicate the endothermic nature of the reaction, so we require energy for further hydrogenate the CO^* intermediate on the surface of the 2D single layer V_N -d-BN material. This higher positive value of ΔG signifies a weak hydrogen binding on the surface of V_N -d-BN material, which will create difficulty in adsorption. Therefore, the higher positive value of ΔG hinders the further hydrogenation of CO^* intermediate. It leads to a thermodynamically unfavorable reaction as a higher applied potential will be required to generate CHO^* and COH^* intermediate along the COOH path.

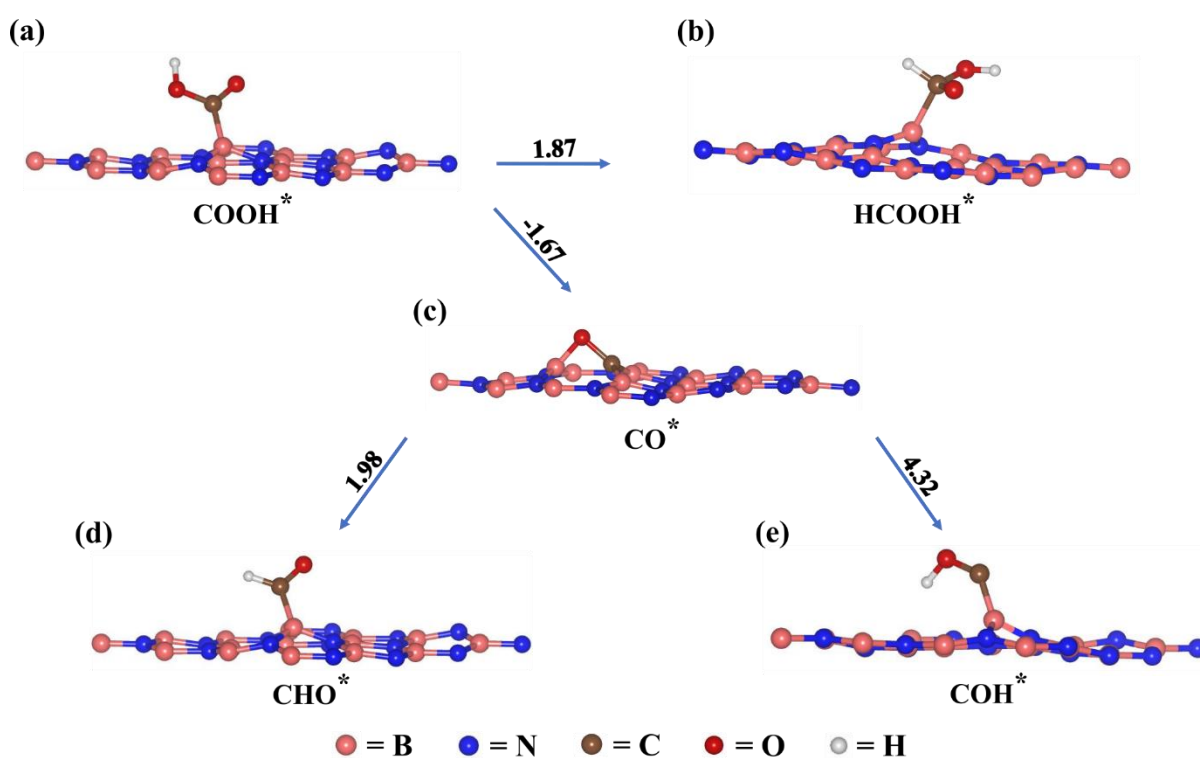


Fig. 4 Formation of HCOOH*, CO*, CHO*, and COH* intermediates on the surface of the 2D monolayer V_N -d-BN material with the equilibrium structures of (a) COOH*, (b) HCOOH*, (c) CO*, (d) CHO*, and (e) COH*.

CO₂RR through the OCHO path

Now, we initiate the CO₂RR using an activated CO₂ molecule on the surface of the V_N -d-BN material for the OCHO path. Fig. 5 shows the equilibrium structures and values of ΔG for possible intermediates of the OCHO path during the CO₂RR process. The first hydrogenation step occurs at the C site of adsorbed CO₂ molecules and splits the C-B bond. Then hydrogen and the carbon atom form a C-H bond, resulting in the formation of an OCHO* intermediate, as shown in Fig. 5b. In this hydrogenation step, we observed a value of ΔG around -1.44 eV for OCHO* intermediate formation, as reported in Table 2. The negative values of ΔG indicate that the reaction step is exothermic and spontaneous. It is important to note here that the value of ΔG for OCHO* formation ($\Delta G = -1.44$ eV) is higher than the value of ΔG for COOH* formation ($\Delta G = -0.50$ eV), so the formation of OCHO* intermediate is considered thermodynamically more favorable. Also, the higher energy released during OCHO* formation indicates the effective activation of the CO₂ molecule on the surface of the 2D monolayer V_N -d-BN material. Therefore, we considered the formation of OCHO* intermediate on the surface of V_N -d-BN material as a primary product for further reduction. The second hydrogenation step occurs at the distantly located O site on the surface of the OCHO* intermediate. This hydrogenation step results in the formation of an OCHOH* intermediate on the catalytic surface, as shown in Fig. 5c. The calculated value of ΔG for this reaction step is 1.80 eV, as reported in Table 2. The positive values of ΔG indicate the endothermic nature of the reaction, so we require energy to hydrogenate the OCHOH* intermediate further on the surface of the V_N -d-BN material. So, this positive change in the value of ΔG provides some resistance to further hydrogenation on the catalytic surface. Still, this path is more favorable than the previously discussed COOH path. Therefore, we consider the formation of an OCHOH* intermediate for further reduction on the surface of the V_N -d-BN material.

In the third hydrogenation step, the hydrogen combines with the distantly located oxygen atom of the O-H site in the OCHOH* intermediate, and the H₂O molecule is desorbed from the catalytic surface. Here, only CHO* remains on the surface of V_N -d-BN material, as shown in Fig. 5d. The calculated value for ΔG is -0.55 eV for CHO* intermediate formation,

as reported in Table 2. The negative value of ΔG indicates the exothermic nature of this reaction step. So, it spontaneously occurs on the catalytic surface. It is important to note that the OCHO path is more favorable than the COOH path here, but at the end of both reaction paths, we get CHO* as a common reaction intermediate. In the fourth hydrogenation step, the hydrogenation of CHO* can lead to the formation of CHOH* and OCH₂* intermediates. Now, if the hydrogen atom bonded to the C site on the surface of the CHO*, it forms an OCH₂* intermediate. But if a hydrogen atom bonded to the O site on the surface of the CHO* intermediate, it forms a CHOH intermediate. The value of ΔG for the CHOH* intermediate formation is calculated to be 1.21 eV, while the value of ΔG for the OCH₂* intermediate formation is around 0.11 eV obtained by the DFT-D method. Here, the change in Gibbs free energies for both the reaction steps is positive, which shows the endothermic nature of the reaction steps of these intermediate states. However, the value of ΔG for the OCH₂* formation is much less than that for the HCOH* formation, so we consider the formation of the OCH₂* intermediate on the surface of V_N_d-BN for further reduction. The equilibrium structure of OCH₂* intermediate on the surface of the 2D monolayer V_N_d-BN material is depicted in Fig. 5e.

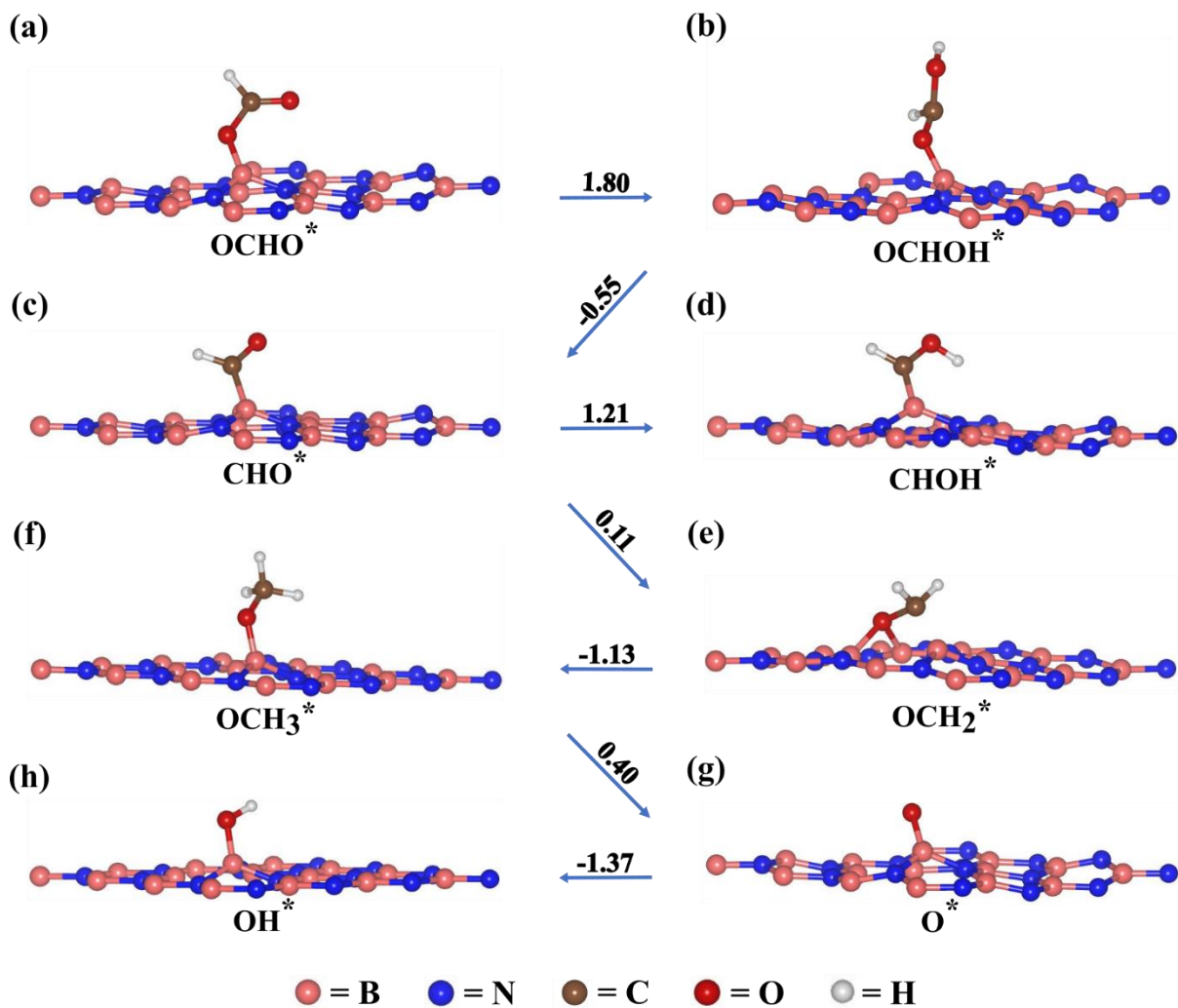


Fig. 5 Adsorption of CO₂ molecule and formation of various intermediates on the surface of 2D monolayer V_N-d-BN material with the equilibrium structures of (a) CO₂*, (b) OCHO*, (c) OCHOH*, (d) CHO*, (e) OCH₂*, (f) OCH₃*, (g) O*, and (h) OH*.

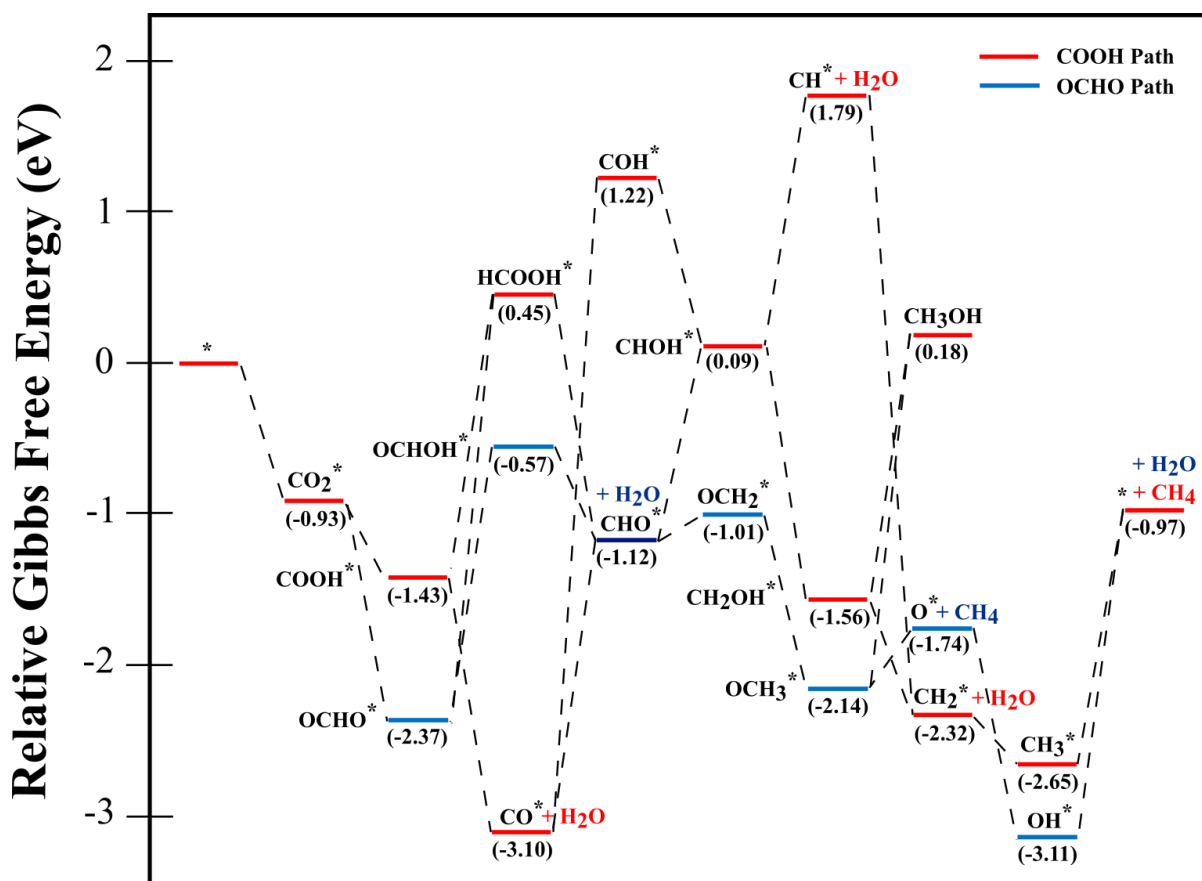
In the fifth hydrogenation step, the intermediate OCH₂* undergoes further hydrogenation, where a hydrogen atom is adsorbed at the C site to form the OCH₃* reaction intermediate. Fig. 5f shows the equilibrium structure of the OCH₃* intermediate on the surface of the 2D monolayer V_N-d-BN material. The calculated value of ΔG for the OCH₃* intermediate formation on the catalytic surface is about -1.13 eV, as reported in Table 2. The negative value of ΔG indicates the exothermic nature of the reaction, which spontaneously occurs on the catalytic surface. In the sixth step, the OCH₃* intermediate can undergo hydrogenation on the surface of the V_N-d-BN material with two possibilities. The first possibility is where hydrogen gets bonded at the O site of the OCH₃* intermediate, which leads to the formation of a CH₃OH molecule. This CH₃OH molecule gets desorbed from the surface of the V_N-d-BN material as a final product. The second possibility is the desorption of a CH₄

molecule from the catalytic surface. Now, only a single oxygen atom remains to produce an H₂O molecule as a final product after two more successive hydrogenation steps. The hydrogenation of the OCH₃* intermediate to form CH₃OH* is accompanied by a value of ΔG around 1.37 eV. In comparison, the formation of the O* intermediate with desorption of the CH₄ molecule has a change in Gibbs free energy around 0.40 eV, as reported in Table 2. The value of ΔG for both steps is positive, which shows the endothermic nature of both reaction steps. The formation of an O* intermediate is more favorable than the desorption of a CH₃OH molecule due to a comparatively smaller value of ΔG . Hence, we consider an O* intermediate with the desorption of a CH₄ molecule on the catalytic surface for further reduction. The optimized structure of O* intermediate on the surface of the 2D monolayer V_N_d-BN material is shown in Fig. 5g.

The intermediate O* undergoes further hydrogenation in the seventh step, where hydrogen bonds with the remaining oxygen on the catalytic surface to form the OH* intermediate, as shown in Fig. 5h. The value of ΔG for this reaction step is around -1.37 eV, as reported in table 2. The negative value of ΔG for OH* formation confirmed the exothermic nature of the reaction, so it occurs spontaneously on the catalytic surface. The remaining OH* intermediate bonded with hydrogen in the last hydrogenation step, forming an H₂O molecule that desorbed from the catalytic surface for the next cycle. The value of ΔG for this hydrogenation step is around 2.18 eV, as reported in Table 2. So, the hydrogenation of OH* is the highly endothermic reaction step and is also considered a rate-limiting step of CO₂RR. The formation of H₂O from the OH* intermediate serves as a crucial step that contributes to the overall reaction and plays a pivotal role in facilitating subsequent cycles of the reaction. The value of change in Gibbs free energy for H₂O formation on the catalytic surface is highly positive, but still, it is a crucial reaction step because it provides an active catalytic surface for the next cycle of CO₂RR. The formation of H₂O at the end of the reaction cycle restores the active sites on the catalytic surface, preparing it for initiating further CO₂RR cycles. The formation of H₂O may create a thermodynamic barrier, but it is a crucial intermediate in restoring the catalyst surface. Therefore, it draws our attention to its importance in sustaining and enhancing the efficiency of CO₂RR processes.

The potential energy surface (PES) diagram illustrates the energetics of the CO₂RR mechanism on the surface of V_N_d-BN material. We present the two prominent paths in the

PES diagram by studying all possible routes. The first is the COOH* path, represented by red color, and the second is the OCHO* path, represented by blue color in the PES diagram, as shown in Fig. 6. Both pathways represent a series of intermediate steps leading to the final product. We can easily understand which path is more thermodynamically favorable by analyzing the relative Gibbs free energies along these CO₂RR pathways. The PES diagram shows which path is more accessible and gives essential information about how likely it will happen. This analysis showed us that the OCHO* path exhibits more favorable than the COOH* path. This conclusion results from observing the change in Gibbs free energy for the formation of each reaction intermediate along both paths. Consequently, the OCHO* path emerges as the preferred route for the CO₂RR process on the surface of the 2D monolayer V_N_d-BN material. Various factors, such as the specific electronic and structural properties of the 2D monolayer V_N_d-BN material, favorably influence the adsorption and activation of CO₂ molecules and intermediates along the OCHO* path. Thoroughly analyzing the PES diagram with the react pathways offers valuable insights into how the CO₂RR process happens on the surface of V_N_d-BN material. It highlights the importance of the OCHO* path in reacting toward favorable results which is accord with the experimental observation performed by Katerina et al.⁴⁰



Reaction Pathway

Fig. 6 Relative Gibbs free energy diagram for the CO₂RR on the surface of the 2D monolayer V_{N_d}-BN material.

Table 1 Equilibrium structural parameters, lattice constants, and electronic band gap (E_g) parameters of various systems of the CO₂RR.

Reaction intermediate	Lattice parameters (Å)	Interfacial angles in degree	Space group & symmetry	Electronic band gap (E_g in eV)	Average bond distance (in Å)				
					B-C	B-O	C-O	C-H	O-H
CO ₂ *	a = 7.509, b = 7.540	$\alpha = \beta = 90$ $\gamma = 120.480$	<i>PI</i>	0	1.591	1.392	1.292	-	-
OCHO*	a = 7.215, b = 7.472	$\alpha = \beta = 90$ $\gamma = 118.882$	<i>PI</i>	5.30	-	1.417	1.281	1.096	-
OCHOH*	a = 7.209, b = 7.476	$\alpha = \beta = 90$ $\gamma = 118.879$	<i>PI</i>	0	-	1.382	1.374	1.091	0.971
CHO*	a = 7.259, b = 7.474	$\alpha = \beta = 90$ $\gamma = 119.041$	<i>PI</i>	0	1.604	-	1.228	1.113	-
OCH ₂ *	a = 7.361,	$\alpha = \beta = 90$	<i>PI</i>	0	1.576	1.559	1.470	1.089	-

	b = 7.549	$\gamma = 119.192$							
OCH ₃ *	a = 7.497, b = 7.497	$\alpha = \beta = 90$ $\gamma = 120.000$	PI	0	-	1.390	1.417	1.092	-
O*	a = 7.209, b = 7.483	$\alpha = \beta = 90$ $\gamma = 118.796$	PI	1.68	-	1.360	-	-	-
OH*	a = 7.497, b = 7.497	$\alpha = \beta = 90$ $\gamma = 120.000$	PI	0	-	1.396	-	-	0.968

Table 2 Change in Gibbs free energy (ΔG in eV) and relative Gibbs free energy of all the intermediates during the CO₂RR performed on the surface of the 2D monolayer V_N_d-BN material is reported here.

Various CO ₂ RR Steps	ΔG (eV)	Relative free energy (eV)
V _N _d-BN* → CO ₂ *	-0.93	-0.93
CO ₂ * → OCHO*	-1.44	-2.37
OCHO* → OCHOH*	1.80	-0.57
OCHOH* → CHO* + H ₂ O	-0.55	-1.12
CHO* → OCH ₂ *	0.11	-1.01
OCH ₂ * → OCH ₃ *	-1.13	-2.14
OCH ₃ * → O* + CH ₄	0.40	-1.74
O* → OH*	-1.37	-3.11
OH* → V _N _d-BN* + H ₂ O	2.14	-0.97

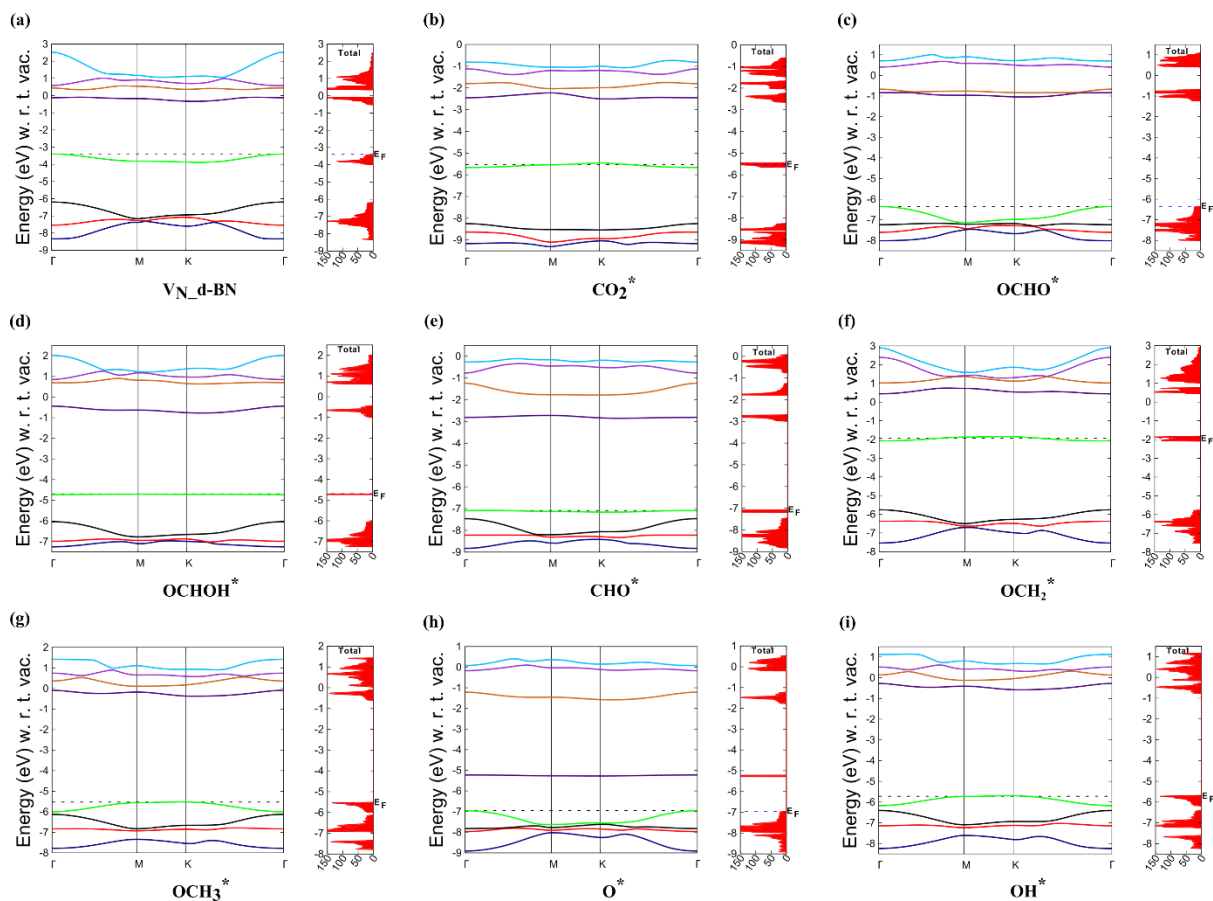


Fig. 7 Schematic illustration of the electronic band structures and total density of states of the 2D monolayer $V_N_d\text{-BN}$ material and all the reaction intermediates along the OCHO path during CO_2RR process are plotted here: (a) $V_N_d\text{-BN}$, (b) CO_2^* , (c) OCHO^* , (d) OCHOH^* , (e) CHO^* , (f) OCH_2^* , (g) OCH_3^* , (h) O^* , and (i) OH^*

In our investigation of the CO_2RR mechanism on the surface of the 2D monolayer $V_N_d\text{BN}$ material, we employed the DFT-D method to explore the electronic properties to understand the catalytic activity of the material. Specifically, we focused on the band structure, electronic band gap (E_g), Fermi energy (E_F) level, and total density of states (DOS) for the $V_N_d\text{-BN}$ material and each reaction intermediate along the OCHO path during CO_2RR . The band structure analysis helps us understand the electronic behavior of a material, highlighting its potential for catalytic activity. Meanwhile, the DOS calculations provide detailed information on the density of electronic states, helping us to observe the availability and distribution of electronic states. To precisely represent the electronic structure, we selected the k-vector path along the highly symmetric directions, named $\Gamma\text{-M-M-}\Gamma$, within the first Brillouin zone for band structure plots. Using the band structure calculations, we have plotted eight electronic energy bands. Four out of these eight energy bands lying above the Fermi energy (E_F) level are named conduction bands, whereas the remaining four lying below the

Fermi energy level are named valence bands. The Fermi energy (E_F) level is represented by the dotted blue line in the computed band structures and DOS calculations as depicted in Figure 7a-I for all the reaction intermediates involved in the subject reaction along with the 2D monolayer V_N _dBN material. We have computed the value of Fermi energy level (E_F) at -3.39 eV in the electronic band structures and total DOS of the 2D monolayer V_N _d-BN material, as shown in Fig. 7a. We observed a tiny fraction of electron density in the total DOS calculations just below the Fermi energy level.

In the electronic band structure calculations, during the initial hydrogenation step, where the CO_2 molecule adsorbs on the surface of the V_N _d-BN material, the Fermi energy (E_F) level shifts toward the conduction band. Eventually, one of the electronic energy bands belonging to the conduction bands crosses the Fermi energy (E_F) level, indicating a conductive nature of CO_2^* . The DOS calculations reveal a substantial electron density of states around the Fermi level (E_F), which also confirms the conductive nature of CO_2^* reaction intermediate formed during the CO_2RR , as shown in Fig. 7b. This characteristic promotes electron propagation during the reaction, and it helps to improve the efficiency of the CO_2RR mechanism. This conductive nature is observed consistently in the further hydrogenation steps involving $OCHOH^*$, CHO^* , OCH_2^* , OCH_3^* , and OH^* on the surface of the 2D monolayer V_N _d-BN material, as shown in Fig. 7d, 7e, 7f, 7g, and 7i, respectively. We observe similar trends in the electronic band structure calculations of these intermediate states, where one of the electronic energy bands of the valence bands shifts towards the Fermi energy level and crosses it, confirming the conductive nature of these intermediates. We also calculated the total DOS for these intermediates and observed the electron density around the Fermi energy level, which also indicates the conductive nature of these intermediates. We also computed the electronic band structure and total DOS of the remaining intermediates formed during the CO_2RR . The electronic band structure calculations of the reaction intermediates $OCHO^*$ and O^* reaction steps reveal the presence of an energy bandgap in these systems, as shown in Fig. 7c and 7h, respectively. In the DOS calculations, we observed a small fraction of electron density just below the Fermi energy level for these systems. Fig. 7a-i shows the electronic band structure and total DOS of the 2D monolayer V_N _d-BN material along all the reaction intermediates involved in the subject reaction. Fig. 6 illustrates the PES diagram, in which we present the relative Gibbs free energies of the two prominent reaction pathways ($COOH$ and $OCHO$) of the CO_2RR mechanism on the surface of the 2D monolayer V_N _d-BN material. Table 1 provides a detailed comparison of various reaction intermediates throughout the

CO₂RR process, including their equilibrium lattice constants, space group symmetry, shift of Fermi energy level, electronic band gap, and average bond lengths. Table 2 presents the change in Gibbs free energy (ΔG) and relative Gibbs free energy for each intermediate involved in the CO₂RR process performed on the surface of the 2D single layer V_N_d-BN material.

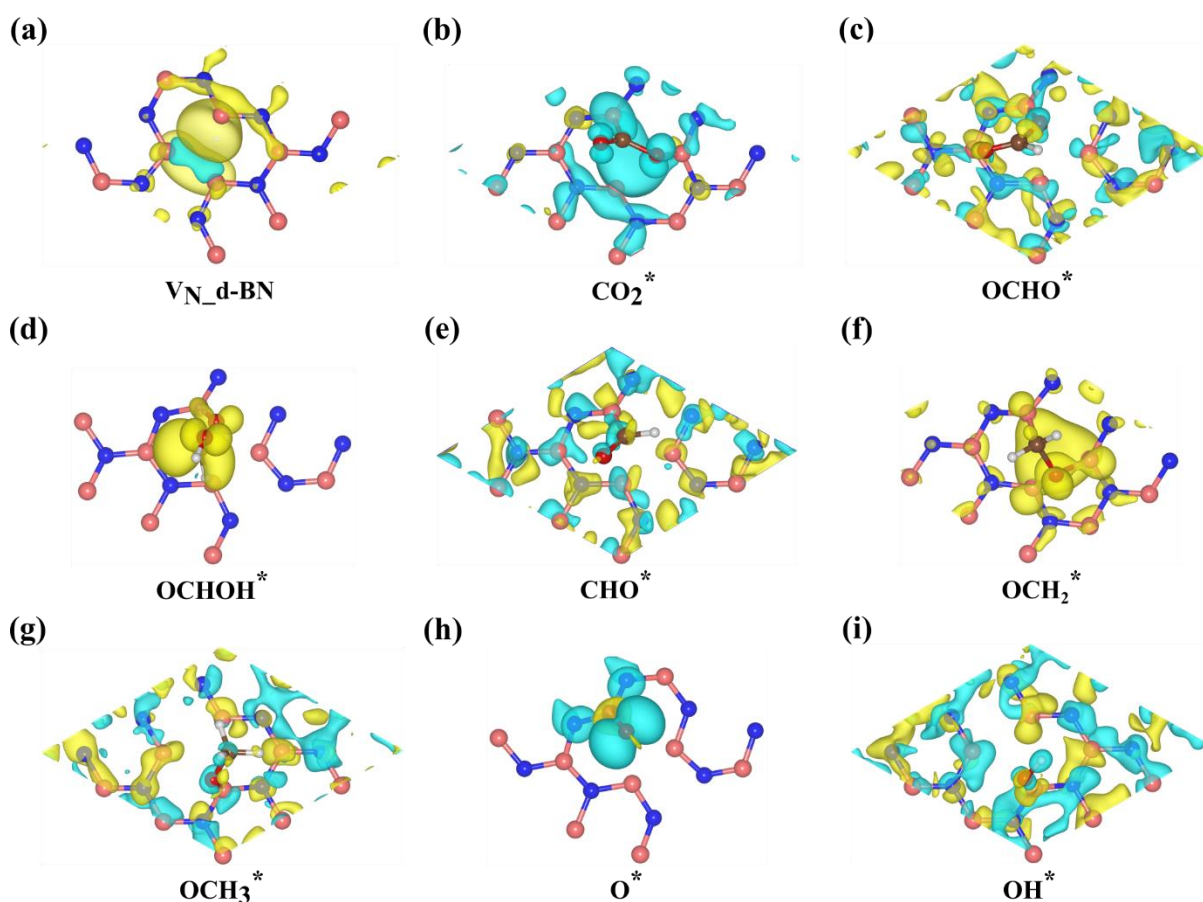


Fig. 8 Electron spin density calculations of V_N_d-BN material and all intermediates formed along the OCHO path during the CO₂RR process: (a) V_N_d-BN, (b) CO₂^{*}, (c) OCHO^{*}, (d) OCHOH^{*}, (e) CHO^{*}, (f) OCH₂^{*}, (g) OCH₃^{*}, (h) O^{*} and (i) OH^{*}.

In this study, we also calculated the electron spin densities of the 2D single layer V_N_d-BN material along all the intermediate states formed during the CO₂RR process by using the same DFT-D method, as depicted in Fig. 8. The electron spin densities offer crucial insights into the electronic structure and reactivity of these systems, which are essential for understanding their catalytic activity towards the CO₂RR. The significance of these calculations lies in their ability to elucidate the distribution of unpaired electrons, which directly influences the reactivity of materials. The distribution of electron spin density is crucial to show how the spin polarization is within the molecular orbitals. The analysis of spin densities

unveils distinct patterns of electron localization and delocalization, highlighting the pivotal role of adsorption sites on the surface of V_N -d-BN material in modulating electron transfer kinetics. The spin density represents the mismatch between the numbers of spin-up (α) and spin-down (β) electrons employed to estimate the presence of unpaired electrons. Under these conditions of unequal distribution of spin-up and spin-down electrons, spin polarization comes into the picture, which also results in non-zero spin density. The spin density functional theory (SDFT) extends DFT to include magnetic fields alongside scalar external potentials from the nuclei. Two space functions, spin density (s) and electron density (ρ), serve as fundamental variables in SDFT. The spin density reflects interactions among electron spins within a system and plays a crucial role in understanding the magnetic phenomena of the material.⁵⁶ In Fig. 8, the α -spin electrons, i.e., the positive component of the electronic wave function, are represented by the highlighted yellow color, while the β -spin electrons, i.e., the negative component of the electronic wave function, are represented by the sky-blue color. The spin density distribution within a molecule is crucial for understanding the propagation of spin polarization in molecular complexes and crystals. It is helpful to understand various magnetic interactions, which are a function of molecular orientation as well as packing. Hence, we can say that electron density plays a crucial role in electrocatalysis during the CO_2RR to facilitate electron transfer in the reaction mechanism.

Conclusions

In our current work, we have investigated the electrocatalytic activities of the defective 2D monolayer hexagonal boron nitride (d-BN) towards CO_2RR which is consistent with the experimental observation. By introducing a single nitrogen-vacancy (V_N) defect in the pristine 2D monolayer hBN, we have examined the electrocatalytic activity of the 2D single layer V_N -d-BN material towards the CO_2RR . We have simulated the Raman spectroscopy of the V_N -d-BN material to determine its overall stability to perform the CO_2RR . We have followed the DFT-D method to computationally explore the structural and electronic properties of the 2D monolayer V_N -d-BN material as well as for all the intermediate states formed during the CO_2RR . We have calculated the electronic properties of the V_N -d-BN material towards all the possible reaction intermediates formed during the CO_2RR , including its band structure and total DOS at the equilibrium position. The findings of our current work suggest that after the introduction of the V_N defect in the pristine 2D monolayer hBN, the electronic band gap of the

2D monolayer V_N -d-BN material is reduced to 3.0 eV. After determining the stable configuration and electronic properties of the V_N -d-BN material, we have explored various possible reaction pathways and primary reduction products involved in the CO_2RR . In the present investigation, we have considered a periodic structural slab structure of the V_N -d-BN material and CO_2RR process has been investigated based on the computational hydrogen electrode (CHE). We have also calculated the electron spin density of all the systems which helps us to locate the unpaired electrons around the defective region of the V_N -d-BN material. This DFT-D approach was consistently applied throughout the calculations to the precise depth of Gibbs free energy during the CO_2RR process. We have explored the two prominent reaction pathways such as $COOH^*$ and $OCHO^*$ on the surface of the 2D single layer V_N -d-BN material. Both the reaction pathways represent a series of intermediate steps leading to the final product. The results of our analysis showed that the $OCHO^*$ path exhibits more favorable than the $COOH^*$ path. Also, we found that the 2d monolayer V_N -d-BN material is more likely to generate CH_4 as the final product rather than CO , $HCOOH$, and CH_3OH during the CO_2RR process. The hydrogenation of OH^* intermediate is the rate-limiting step. Overall, the V_N -d-BN material demonstrates significant activity and selectivity as an electrocatalyst for the reduction of CO_2 to CH_4 . Hence, the 2D monolayer V_N -d-BN exhibits promising electrocatalytic activity for CO_2RR with substantially improved reaction kinetics.

Conflicts of Interest:

The authors have no additional conflicts of interest.

AUTHOR INFORMATION

Corresponding Author

Dr. Srimanta Pakhira – *Theoretical Condensed Matter Physics and Advanced Computational Materials Science Laboratory, Department of Physics, Indian Institute of Technology Indore (IIT Indore), Simrol, Khandwa Road, Indore, Madhya Pradesh 453552, India.*

Theoretical Condensed Matter Physics and Advanced Computational Materials Science Laboratory, Centre of Advanced Electronics (CAE), Indian Institute of Technology Indore, Indore, MP 453552, India.

ORCID: orcid.org/0000-0002-2488-300X.

Email: spakhira@iiti.ac.in or spakhirafsu@gmail.com

Authors

Mr. Lokesh Yadav – *Theoretical Condensed Matter Physics and Advanced Computational Materials Science Laboratory, Department of Physics, Indian Institute of Technology Indore (IIT Indore), Simrol, Khandwa Road, Indore, Madhya Pradesh 453552, India.*

Acknowledgement:

This work was financially supported by the Science and Engineering Research Board-Department of Science and Technology (SERB-DST), Government of India, under Grant No. CRG/2021/000572. We thank the CSIR, Govt of India for providing the research funds under the scheme no. 22/0883/23/EMR-II. Dr Srimanta Pakhira acknowledges the SERB-DST, Government of India, for providing his Early Career Research Award (ECRA) under project number ECR/2018/000255 and for providing the computer cluster. Dr Pakhira also recognizes the SERB-DST for providing the highly prestigious Ramanujan Faculty Fellowship under scheme number SB/S2/RJN-067/2017 and providing the highly prestigious Core Research Grant (CRG), SERB-DST, Govt. of India under the scheme number CRG/2021/000572. Ms. Lokesh thanks the CSIR, Govt. of India, and Govt. of India for providing his doctoral fellowship under scheme no. CSIRAWARD/JRF-NET2022/11898. The author would like to acknowledge the SERB-DST for providing computing clusters and programs.

Author Contributions:

Dr. Pakhira designed the project, and he conceived the complete idea of this current research project work, Mr. Lokesh Yadav computationally studied the electronic structures and properties of the 2D monolayer hBN and V_N -d-BN materials. Dr. Pakhira and Mr. Lokesh Yadav explored the whole reaction paths, transition states, and reaction barriers. They explained the CO₂RR mechanism by the DFT Quantum Mechanical calculations. Dr. Pakhira and Mr. Lokesh wrote the whole manuscript and prepared all the tables and figures in the manuscript. Dr. Pakhira and Mr. Lokesh interpreted and analyzed the computed results, and Dr. Pakhira supervised the project work.

References:

- (1) Caldeira, K.; Wickett, M. E. Anthropogenic Carbon and Ocean PH. *Nature* **2003**, *425*,

365.

- (2) Masson-Delmotte, V.; Kageyama, M.; Braconnot, P.; Charbit, S.; Krinner, G.; Ritz, C.; Guilyardi, E.; Jouzel, J.; Abe-Ouchi, A.; Crucifix, M.; Gladstone, R. M.; Hewitt, C. D.; Kitoh, A.; LeGrande, A. N.; Marti, O.; Merkel, U.; Motoi, T.; Ohgaito, R.; Otto-Bliesner, B.; Peltier, W. R.; Ross, I.; Valdes, P. J.; Vettoretti, G.; Weber, S. L.; Wolk, F.; YU, Y. Past and Future Polar Amplification of Climate Change: Climate Model Intercomparisons and Ice-Core Constraints. *Clim. Dyn.* **2006**, *26*, 513–529.
- (3) White, J. W. C.; Ciais, P.; Figge, R. A.; Kenny, R.; Markgraf, V. A High-Resolution Record of Atmospheric CO₂ Content from Carbon Isotopes in Pet. *Nature* **1994**, *367*, 153–156.
- (4) Li, M.; Wang, H.; Luo, W.; Sherrell, P. C.; Chen, J.; Yang, J. Heterogeneous Single-Atom Catalysts for Electrochemical CO₂ Reduction Reaction. *Adv. Mater.* **2020**, *32*, 2001848.
- (5) Wang, G.; Chen, J.; Ding, Y.; Cai, P.; Yi, L.; Li, Y.; Tu, C.; Hou, Y.; Wen, Z.; Dai, L. Electrocatalysis for CO₂ Conversion: From Fundamentals to Value-Added Products. *Chem. Soc. Rev.* **2021**, *50*, 4993–5061.
- (6) Graves, C.; Ebbesen, S. D.; Mogensen, M.; Lackner, K. S. Sustainable Hydrocarbon Fuels by Recycling CO₂ and H₂O with Renewable or Nuclear Energy. *Renew. Sustain. Energy Rev.* **2011**, *15*, 1–23.
- (7) Centi, G.; Quadrelli, E. A.; Perathoner, S. Catalysis for CO₂ Conversion: A Key Technology for Rapid Introduction of Renewable Energy in the Value Chain of Chemical Industries. *Energy & Environ. Sci.* **2013**, *6*, 1711–1731.
- (8) Kumar, B.; Llorente, M.; Froehlich, J.; Dang, T.; Sathrum, A.; Kubiak, C. P. Photochemical and Photoelectrochemical Reduction of CO₂. *Annu. Rev. Phys. Chem.* **2012**, *63*, 541–569.
- (9) Mikkelsen, M.; Jørgensen, M.; Krebs, F. C. The Teraton Challenge. A Review of Fixation and Transformation of Carbon Dioxide. *Energy & Environ. Sci.* **2010**, *3*, 43–81.
- (10) Roy, S. C.; Varghese, O. K.; Paulose, M.; Grimes, C. A. Toward Solar Fuels: Photocatalytic Conversion of Carbon Dioxide to Hydrocarbons. *ACS Nano* **2010**, *4*,

- 1259–1278.
- (11) Whipple, D. T.; Kenis, P. J. A. Prospects of CO₂ Utilization via Direct Heterogeneous Electrochemical Reduction. *J. Phys. Chem. Lett.* **2010**, *1*, 3451–3458.
 - (12) Wang, W.; Wang, S.; Ma, X.; Gong, J. Recent Advances in Catalytic Hydrogenation of Carbon Dioxide. *Chem. Soc. Rev.* **2011**, *40*, 3703–3727.
 - (13) Costentin, C.; Robert, M.; Savéant, J.-M. Catalysis of the Electrochemical Reduction of Carbon Dioxide. *Chem. Soc. Rev.* **2013**, *42*, 2423–2436.
 - (14) Zhan, Z.; Zhao, L. Electrochemical Reduction of CO₂ in Solid Oxide Electrolysis Cells. *J. Power Sources* **2010**, *195*, 7250–7254.
 - (15) Jhong, H.-R. “Molly”; Ma, S.; Kenis, P. J. A. Electrochemical Conversion of CO₂ to Useful Chemicals: Current Status, Remaining Challenges, and Future Opportunities. *Curr. Opin. Chem. Eng.* **2013**, *2*, 191–199.
 - (16) Lu, Q.; Jiao, F. Electrochemical CO₂ Reduction: Electrocatalyst, Reaction Mechanism, and Process Engineering. *Nano Energy* **2016**, *29*, 439–456.
 - (17) Sun, Z.; Ma, T.; Tao, H.; Fan, Q.; Han, B. Fundamentals and Challenges of Electrochemical CO₂ Reduction Using Two-Dimensional Materials. *Chem* **2017**, *3*, 560–587.
 - (18) Wang, H.; Yuan, H.; Hong, S. S.; Li, Y.; Cui, Y. Physical and Chemical Tuning of Two-Dimensional Transition Metal Dichalcogenides. *Chem. Soc. Rev.* **2015**, *44*, 2664–2680.
 - (19) Deng, D.; Novoselov, K. S.; Fu, Q.; Zheng, N.; Tian, Z.; Bao, X. Catalysis with Two-Dimensional Materials and Their Heterostructures. *Nat. Nanotechnol.* **2016**, *11*, 218–230.
 - (20) Sheng, W.; Amin, I.; Neumann, C.; Dong, R.; Zhang, T.; Wegener, E.; Chen, W.-L.; Förster, P.; Tran, H. Q.; Löffler, M.; others. Polymer Brushes on Hexagonal Boron Nitride. *Small* **2019**, *15*, 1805228.
 - (21) Ares, P.; Cea, T.; Holwill, M.; Wang, Y. B.; Roldán, R.; Guinea, F.; Andreeva, D. V.; Fumagalli, L.; Novoselov, K. S.; Woods, C. R. Piezoelectricity in Monolayer Hexagonal Boron Nitride. *Adv. Mater.* **2020**, *32*, 1905504.
 - (22) Holmes, S. M.; Balakrishnan, P.; Kalangi, V. S.; Zhang, X.; Lozada-Hidalgo, M.;

- Ajayan, P. M.; Nair, R. R. 2D Crystals Significantly Enhance the Performance of a Working Fuel Cell. *Adv. Energy Mater.* **2017**, *7*, 1601216.
- (23) Qian, G. L.; Xie, Q.; Liang, Q.; Luo, X. Y.; Wang, Y. X. Electronic Properties and Photocatalytic Water Splitting with High Solar-to-Hydrogen Efficiency in a HBNC/Janus WSSe Heterojunction: First-Principles Calculations. *Phys. Rev. B* **2023**, *107*, 155306.
- (24) Santos, J.; Moschetta, M.; Rodrigues, J.; Alpuim, P.; Capasso, A. Interactions between 2D Materials and Living Matter: A Review on Graphene and Hexagonal Boron Nitride Coatings. *Front. Bioeng. Biotechnol.* **2021**, *9*, 612669.
- (25) Denis, P. A.; Ullah, S.; Iribarne, F. Reduction Chemistry of Hexagonal Boron Nitride Sheets and Graphene: A Comparative Study on the Effect of Alkali Atom Doping on Their Chemical Reactivity. *New J. Chem.* **2020**, *44*, 5725–5730.
- (26) Liao, Y.; Chen, Z.; Connell, J.; Lin, Y. Chemistry of Boron Nitride Nanosheets. *Nanotub. Nanosheets, CRC Press.* **2015**, 367–408.
- (27) Ikeda, T.; Boero, M.; Huang, S.-F.; Terakura, K.; Oshima, M.; Ozaki, J.; Miyata, S. Enhanced Catalytic Activity of Carbon Alloy Catalysts Codoped with Boron and Nitrogen for Oxygen Reduction Reaction. *J. Phys. Chem. C* **2010**, *114*, 8933–8937.
- (28) Lyalin, A.; Nakayama, A.; Uosaki, K.; Taketsugu, T. Theoretical Predictions for Hexagonal BN Based Nanomaterials as Electrocatalysts for the Oxygen Reduction Reaction. *Phys. Chem. Chem. Phys.* **2013**, *15*, 2809–2820.
- (29) Lyalin, A.; Nakayama, A.; Uosaki, K.; Taketsugu, T. Functionalization of Monolayer H-BN by a Metal Support for the Oxygen Reduction Reaction. *J. Phys. Chem. C* **2013**, *117*, 21359–21370.
- (30) Solozhenko, V. L.; Lazarenko, A. G.; Petitet, J.-P.; Kanaev, A. V. Bandgap Energy of Graphite-like Hexagonal Boron Nitride. *J. Phys. Chem. Solids* **2001**, *62*, 1331–1334.
- (31) Golberg, D.; Bando, Y.; Huang, Y.; Terao, T.; Mitome, M.; Tang, C.; Zhi, C. Boron Nitride Nanotubes and Nanosheets. *ACS Nano* **2010**, *4*, 2979–2993.
- (32) Zhou, J.; Wang, Q.; Sun, Q.; Jena, P. Electronic and Magnetic Properties of a BN Sheet Decorated with Hydrogen and Fluorine. *Phys. Rev. B* **2010**, *81*, 85442.

- (33) Huang, C.; Ye, X.; Chen, C.; Lin, S.; Xie, D. A Computational Investigation of CO Oxidation on Ruthenium-Embedded Hexagonal Boron Nitride Nanosheet. *Comput. Theor. Chem.* **2013**, *1011*, 5–10.
- (34) Lin, S.; Ye, X.; Johnson, R. S.; Guo, H. First-Principles Investigations of Metal (Cu, Ag, Au, Pt, Rh, Pd, Fe, Co, and Ir) Doped Hexagonal Boron Nitride Nanosheets: Stability and Catalysis of CO Oxidation. *J. Phys. Chem. C* **2013**, *117*, 17319–17326.
- (35) Fan, M.; Jimenez, J. D.; Shirodkar, S. N.; Wu, J.; Chen, S.; Song, L.; Royko, M. M.; Zhang, J.; Guo, H.; Cui, J.; others. Atomic Ru Immobilized on Porous h-BN through Simple Vacuum Filtration for Highly Active and Selective CO₂ Methanation. *ACS Catal.* **2019**, *9*, 10077–10086.
- (36) Sun, W.; Meng, Y.; Fu, Q.; Wang, F.; Wang, G.; Gao, W.; Huang, X.; Lu, F. High-Yield Production of Boron Nitride Nanosheets and Its Uses as a Catalyst Support for Hydrogenation of Nitroaromatics. *ACS Appl. Mater. & interfaces* **2016**, *8*, 9881–9888.
- (37) Fang, C.; An, W. Single-Metal-Atom Site with High-Spin State Embedded in Defective BN Nanosheet Promotes Electrocatalytic Nitrogen Reduction. *Nano Res.* **2021**, *14*, 4211–4219.
- (38) Zhao, J.; Chen, Z. Single Mo Atom Supported on Defective Boron Nitride Monolayer as an Efficient Electrocatalyst for Nitrogen Fixation: A Computational Study. *J. Am. Chem. Soc.* **2017**, *139*, 12480–12487.
- (39) Lei, Y.; Pakhira, S.; Fujisawa, K.; Liu, H.; Guerrero-Bermea, C.; Zhang, T.; Dasgupta, A.; Martinez, L. M.; Rao Singamaneni, S.; Wang, K.; Shallenberger, J.; Elías, A. L.; Cruz-Silva, R.; Endo, M.; Mendoza-Cortes, J. L.; Terrones, M. Low Temperature Activation of Inert Hexagonal Boron Nitride for Metal Deposition and Single Atom Catalysis. *Mater. Today* **2021**, *51*, 108–116.
- (40) Chagoya, K. L.; Nash, D. J.; Jiang, T.; Le, D.; Alayoglu, S.; Idrees, K. B.; Zhang, X.; Farha, O. K.; Harper, J. K.; Rahman, T. S.; others. Mechanically Enhanced Catalytic Reduction of Carbon Dioxide over Defect Hexagonal Boron Nitride. *ACS Sustain. Chem. & Eng.* **2021**, *9*, 2447–2455.
- (41) Yadav, L.; Pakhira, S. Platinum-Adsorbed Defective 2D Monolayer Boron Nitride: A Promising Electrocatalyst for O₂ Reduction Reaction. *J. Mater. Chem. C* **2023**, *11*,

- 15215–15232.
- (42) Antony, J.; Grimme, S. Density Functional Theory Including Dispersion Corrections for Intermolecular Interactions in a Large Benchmark Set of Biologically Relevant Molecules. *Phys. Chem. Chem. Phys.* **2006**, *8*, 5287–5293.
- (43) Dovesi, R.; Pascale, F.; Civalleri, B.; Doll, K.; Harrison, N. M.; Bush, I.; D’arco, P.; Noël, Y.; Rérat, M.; Carbonnière, P.; others. The CRYSTAL Code, 1976--2020 and beyond, a Long Story. *J. Chem. Phys.* **2020**, *152*, 204111.
- (44) Pakhira, S.; Sahu, C.; Sen, K.; Das, A. K. Can Two T-Shaped Isomers of OCS-C₂H₂ van Der Waals Complex Exist? *Chem. Phys. Lett.* **2012**, *549*, 6–11.
- (45) Dovesi, R.; Erba, A.; Orlando, R.; Zicovich-Wilson, C. M.; Civalleri, B.; Maschio, L.; Rérat, M.; Casassa, S.; Baima, J.; Salustro, S.; others. Quantum-Mechanical Condensed Matter Simulations with CRYSTAL. *Wiley Interdiscip. Rev. Comput. Mol. Sci.* **2018**, *8*, e1360.
- (46) Laun, J.; Vilela Oliveira, D.; Bredow, T. Consistent Gaussian Basis Sets of Double-and Triple-Zeta Valence with Polarization Quality of the Fifth Period for Solid-State Calculations. *J. Comput. Chem.* **2018**, *39*, 1285–1290.
- (47) Peintinger, M. F.; Oliveira, D. V.; Bredow, T. Consistent Gaussian Basis Sets of Triple-Zeta Valence with Polarization Quality for Solid-State Calculations. *J. Comput. Chem.* **2013**, *34*, 451–459.
- (48) Liang, K.; Pakhira, S.; Yang, Z.; Nijamudheen, A.; Ju, L.; Wang, M.; Aguirre-Velez, C. I.; Sterbinsky, G. E.; Du, Y.; Feng, Z.; others. S-Doped MoP Nanoporous Layer toward High-Efficiency Hydrogen Evolution in PH-Universal Electrolyte. *ACS Catal.* **2018**, *9*, 651–659.
- (49) Pakhira, S.; Mendoza-Cortes, J. L. Tuning the Dirac Cone of Bilayer and Bulk Structure Graphene by Intercalating First Row Transition Metals Using First-Principles Calculations. *J. Phys. Chem. C* **2018**, *122*, 4768–4782.
- (50) Pakhira, S.; Mendoza-Cortes, J. L. Intercalation of First Row Transition Metals inside Covalent-Organic Frameworks (COFs): A Strategy to Fine Tune the Electronic Properties of Porous Crystalline Materials. *Phys. Chem. Chem. Phys.* **2019**, *21*, 8785–8796.

- (51) Upadhyay, S. N.; Halba, D.; Yadav, L.; Pakhira, S. Illuminating the Role of Mo Defective 2D Monolayer MoTe₂ toward Highly Efficient Electrocatalytic O₂ Reduction Reaction. *Langmuir* **2023**, *39*, 17700–17712.
- (52) Grimme, S.; Antony, J.; Ehrlich, S.; Krieg, H. A Consistent and Accurate Ab Initio Parametrization of Density Functional Dispersion Correction (DFT-D) for the 94 Elements H-Pu. *J. Chem. Phys.* **2010**, *132*, 154104.
- (53) Monkhorst, H. J.; Pack, J. D. Special Points for Brillouin-Zone Integrations. *Phys. Rev. B* **1976**, *13*, 5188.
- (54) Momma, K.; Izumi, F. VESTA 3 for Three-Dimensional Visualization of Crystal, Volumetric and Morphology Data. *J. Appl. Crystallogr.* **2011**, *44*, 1272–1276.
- (55) Nørskov, J. K.; Rossmeisl, J.; Logadottir, A.; Lindqvist, L.; Kitchin, J. R.; Bligaard, T.; Jónsson, H. Origin of the Overpotential for Oxygen Reduction at a Fuel-Cell Cathode. *J. Phys. Chem. B* **2004**, *108*, 17886–17892.
- (56) Bruno, G.; Macetti, G.; Lo Presti, L.; Gatti, C. Spin Density Topology. *Molecules* **2020**, *25*, 3537.